

## MUTUAL RELATIONSHIP OF OSCILLATIONS IN THE FREQUENCY RANGE 3.6 mHz TO 22 mHz IN THE SOLAR CHROMOSPHERE

A. Anđić<sup>1,2</sup>

<sup>1</sup>*Institut für Astrophysik,  
Friedrich-Hund-Platz 1, 37077 Göttingen, Germany*

<sup>2</sup>*Faculty of Sciences,  
M. Stojanovića 2, 78000 Banja Luka, Bosnia and Herzegovina*

(Received: February 22, 2006; Accepted: May 19, 2006)

**SUMMARY:** High frequency acoustic oscillations were suggested as the source of mechanical heating in the chromosphere. In this work the radial component of the oscillations in the frequency interval 3 mHz to 22 mHz are investigated. The observations were performed using 2D spectrometry on the Fe I neutral spectral line at 543.45 nm. The high frequency oscillations of different frequencies appear to be associated with different spatial scales. It seems that different sources produce high and low frequency acoustic oscillations.

**Key words.** Sun: chromosphere – Sun: oscillations

### 1. INTRODUCTION

The temperature structure of the chromosphere is interesting. At a height of approximately 500 km there is a temperature minimum around 4200 K. Moving to a height of 2300 km the temperature increases to approximately 10000K (Vernazza et al. 1981). This phenomenon can only be explained by mechanical heating of the chromosphere. During the last century, high frequency acoustic oscillations were suggested as the source of mechanical heating in the chromosphere. Their origin was believed to be in the sub-photosphere, yet connected with the processes in the convection zone. High frequency oscillations with periods from 6 mHz to 100 mHz are assumed to be the main carrier of the required energy and the heating should balance the radiative loss (Kalkofen 2001). The existence of the chromosphere and corona depend on a constant energy supply provided by mechanical heating mechanisms (Ulmschneider and Kalkofen 2002).

The generation of acoustic oscillations can be described by the 'Lighthill mechanism' (Lighthill 1951). Acoustic oscillations appear to be generated by turbulent eddies for which the dissipation of kinetic energy by viscosity is negligible (Proudman 1952). The majority of acoustic oscillations must originate from isolated sources which occupy relatively small volumes of space. There are several possibilities how the convection zone may generate the wave modes in the atmosphere: a) convective motions penetrate into atmospheric layers and directly deposit their energy; b) pressure fluctuations, generated by convective motions, propagate as acoustic oscillations; c) thermal over-stabilities, which occur in the upper layers of the convection zone, generate oscillations (Kalkofen 1990). Some authors argue that high frequency bursts are either generated by rising granules, or propagate more or less uniformly from deeper layers into the convection zone (Deubner and Laufer 1983). The acoustic events that generate 3 mHz oscillations should also produce 5 mHz oscilla-

tions (Hoekzema et al. 2002). Although there is a general consensus that the source of acoustic oscillations is convective motion, some authors argue that one can not decide whether their origin is convective or magnetic. The observational and theoretical results do not reveal a clear picture of the source of solar oscillations (Moretti et al. 2001).

The most energetic oscillations should be generated in those regions where the convective velocities are largest. The energy emission is sensitive to the Mach number of the turbulence and to the frequency of the oscillations, since the opposite motions at opposite sides of the eddy produce acoustic oscillations which cancel at large distances (Stein 1967). The frequencies of the acoustic oscillations depend on various parameters of the fluid flow (Lighthill 1951). One of the ideas of the Lighthill mechanism is that acoustic oscillations which radiate to large distances and reach the same point simultaneously, are not emitted simultaneously (Lighthill 1951).

Observations (Espagnet et al. 1992) show that the acoustic events occur preferentially in the dark intergranular lanes, i.e. corresponding to down flows of plasma. This leads the authors to the conclusion that the excitation of solar oscillations is associated with a rapid cooling occurring in the upper convection layer. The most energetic oscillations are associated with down-flows in dark areas which are well separated from each other in time and space (Espagnet et al. 1992). Some observers noticed strong oscillations following expansions of intergranular spaces. There is observational evidence that acoustic oscillations tend to be converted into magneto-acoustic oscillations at locations where a magnetic field is expected, e.g., at granular boundaries or in bright points (Espagnet et al. 1992).

The propagation of oscillations through the atmosphere will cause a height-dependent variation of its frequency (Stein and Leibacher 1974, Ulmschneider 2003). These changes are caused by the resonance property, the merging of shocks, and from shocks ‘cannibalising’ each other. As a consequence of this behaviour, an almost pure 3 minute periodicity develops at height of 2000 km. Above 5000 km, the chromosphere reaches a dynamical steady state where the mean temperature is time-independent (Ulmschneider 2003).

## 2. OBSERVATIONS

Data sets used in the analysis of this work were obtained using high-cadence observations of the Fe I neutral spectral line (543.45 nm). The 2D spectroscopy was performed using the German Vacuum Tower telescope (VTT) on the Canary islands, with the “Göttingen” Fabry-Perot spectrometer (Bendlin et al. 1992). From the settings of the post-focus instrument presented in Koschinsky et al. (2001) the polarimeter was not used.

In this work data sets from several observation campaigns were used, five in total. The post-focus instrument is made following the demands of speckle

reconstruction (Bendlin et al. 1992). Therefore it takes simultaneously two types of images, broadband and narrow-band. The broadband images are images of integrated light in the observed spectral line. The narrow-band images are scanned through the spectral line using the Fabry-Perot spectrometer (Bendlin et al. 1992). The images are saved in bursts following the demands of the speckle reconstruction method Boer (1992, 1994). The chosen spectral line was scanned in 13 positions, where two position were in continuum.

The data set, DS1, was taken by J.K. Hirzberger and M. Wunnenberg during August 2000 (Wunnenberg et al. 2003b). The rest of data sets were taken during observational campaign in June 2004 (DS2, DS3, DS4 and DS5). During the 2004 observing run the adaptive optic (Berkefeld and Soltau 2001, Soltau et al. 2002) were used.

**Table 1.** Informations about the data sets used in this work. Sun coordinates present the coordinates of the observed solar area in arc sec, where the referent point is the centre of the Sun, images represent number of images per burst, exposure time represents exposure time per image, while cadence represents the repetition time of bursts.

mark	Sun coordinates	images	exposure time	cadence
DS1	[0, 0]	104	20	25
DS2	[0, 0]	108	30	28.3
DS3	[96.7, 90.7]	91	20	22.7
DS4	[19.8, -45]	91	20	22.7
DS5	[6, 0]	91	20	29.9

The main objective was to achieve the fastest repetition rate possible, allowing to study oscillations with shortest periods. The FWHM of the spectrometer and the step-width were 32.8 m and 31.9 m, respectively. At each wavelength position, a predetermined number of frames with an appropriate exposure time were taken (see Table 1). Broadband images were taken simultaneously with the narrow-band images, since this is necessary for the application of later the speckle reconstruction. Since the time evolution of high frequency oscillations was the main area of interest, reasonably long time sequences were taken, varying from 34min for the data sets with the highest cadence to 50min for the data set with the lowest cadence. Various solar features were observed. The data sets DS1, DS2 and DS3 had quiet sun areas in the field of view, DS5 had G-band structures (G-band is in 429.5 – 431.5 nm spectral range, populated by many spectral lines of the CH molecule and shows the bright features in the intergranular down-flow regions, the so called G-band bright points (Sheylak et al. 2004)) and DS4 has a pore as the object of observation. The data set DS4 is also used as the data set with the G-band structures since in the pore vicinity abnormal granulation and bright points begin to appear. Before this analysis the field of view was divided, the pore itself with its vicinity was cut from field of view, and treated separately.

### 3. DATA REDUCTION AND ANALYSIS METHODS

The data reduction for the broadband images is done with a program developed by P. Sutterlin following the method of de Boer (1992, 1994). The program included the following procedures: subtraction of darks, flat fielding and speckle reconstruction. Speckle reconstruction of the broadband images at each time step was done with the spectral ratio method (von der Lhe 1984) and the speckle masking method (Weigelt 1977). An example of one resulting image is given in Fig. 2.

The program set used for the reconstruction of narrow band images was developed by Janssen (2003) and is based on the method developed by Keller et al. (1992), as described in Krieg et al. (1999) and Hirzberger et al. (2001). From this images the two dimensional Doppler shift fluctuations from bisectors were calculated for each time step. During each burst of the time series, the images from near line centre used for the present study were taken at different times, but with less than 5s separation. I did not correct for this (by rotating in Fourier space to the same position in time).

To reduce the contribution of atmospheric fluctuations to the observed oscillation the velocity response functions (Function which describes from which heights in the atmosphere the information about velocity carried by photons originate.) were calculated. They were calculated using the code developed by F. Kneer following the method of Eibe et al. (2001) and Pérez Rodrigues and Kneer (2002) and using the LTE atmospheric model (Holweger and Müller 1974).

The velocity response functions cover a rather broad interval of heights. The largest contribution to the fluctuations comes from heights between 400 km and 600 km. Thirty response functions are calculated for the intensity levels of bisector from  $I_\lambda = 0.32$  to  $I_\lambda = 0.9$ , where the step width is 0.02. Closer to the core of the line the functions tend to be too broad, covering a wide range of the heights. Therefore linear combinations were used to narrow this contribution. This was achieved by calculating the velocity response functions:

$$RF_{v(z_{600})} = \frac{RF_0 - 0.6RF_4}{0.4} \quad (1)$$

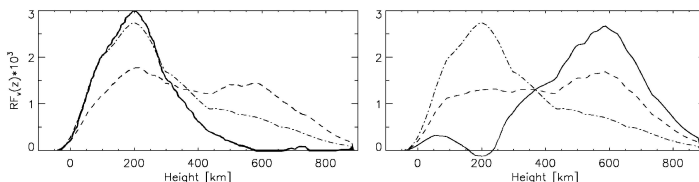


**Fig. 1.** Linear combinations of velocity response functions for the spectral line 543.45 nm. The left panel shows the combination yielding a maximum at 200 km and the right at 600 km. Resulting velocity response on both panels is presented as a solid line, while on the left panel the dashed line represents the velocity response function from bisector level 5, and the dot-dashed line from bisector level 2. On the right panel, the dashed line represent the velocity response function from bisector level 4 and the dot-dashed line from level 0.

$$RF_{v(z_{200})} = \frac{RF_5 - 0.7RF_2}{0.3} \quad (2)$$

where  $RF_i$  represents the velocity response function for the corresponding bisector level  $i$ . The results of the calculations are shown in Fig. 1.

The response functions are normalised to give:

$$\int_{-\infty}^{+\infty} RF_v(z) dz = 1, \quad (3)$$

where  $z$  represent height along the bisector.

The initial assumption is the signals are small and use the same combination as above to produce new velocity images. It turns out that the velocities are of the order of  $1 km/s^{-1}$ . This exceeds slightly the linear regime required by the response functions. More accurate determinations must be deferred until I have performed thorough tests with this method. The simulations of large amplitude oscillations, shocks and their expected signals in our apparatus must be performed with correct radiative transfer solutions.

In order to study the time evolution, additional correlation and de-stretching was performed. For this procedure the code developed by Yi and Molowny Horas (1992), following the method of November (1986) is used.

The signal of lower frequency oscillations is stronger than the signal of high frequency oscillations, providing a need for wavelet analysis techniques. The 3D data cubes (two spacial dimensions and one temporal) of the velocity maps (Fig. 3) were subjected to wavelet analysis using a Morlet waveform:

$$\psi_0(t) = \pi^{-\frac{1}{4}} e^{i\omega_0 t} e^{-\frac{t^2}{2}}, \quad (4)$$

where  $\omega_0$  is the non-dimensional frequency and  $t$  the non-dimensional time parameter. The code for the present wavelet analysis is based on the one developed by Torrence and Compo (1998). The code (Torrence and Compo 1998) is made for noncyclic data in Fourier space. To avoid errors at the edges of the data set, apodisation of the data was performed before it was run through the wavelet routine. As a result two dimensional spatial distributions of the oscillations were acquired Fig. 4.

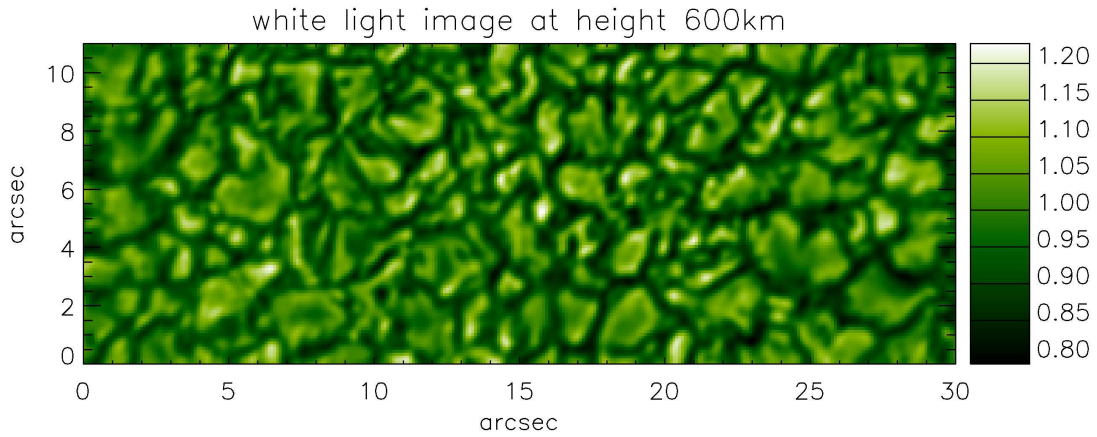


**Fig. 2.** The example of the white light image at a height of 600 km, reconstructed for the data set DS3. The map is corresponding to 113s of the time sequence covered with the data set.

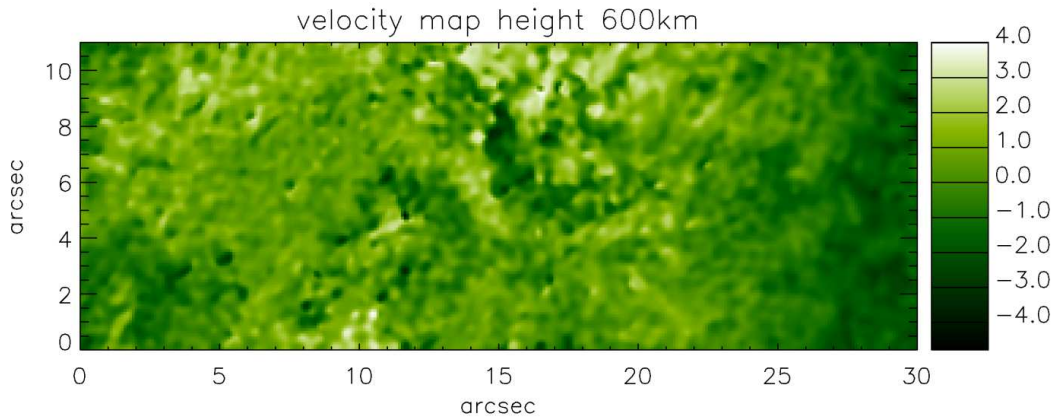


**Fig. 3.** The example of the velocity map at a height of 600 km, calculated for the data set DS3. The map is corresponding to 113s of the time sequence covered with the data set.

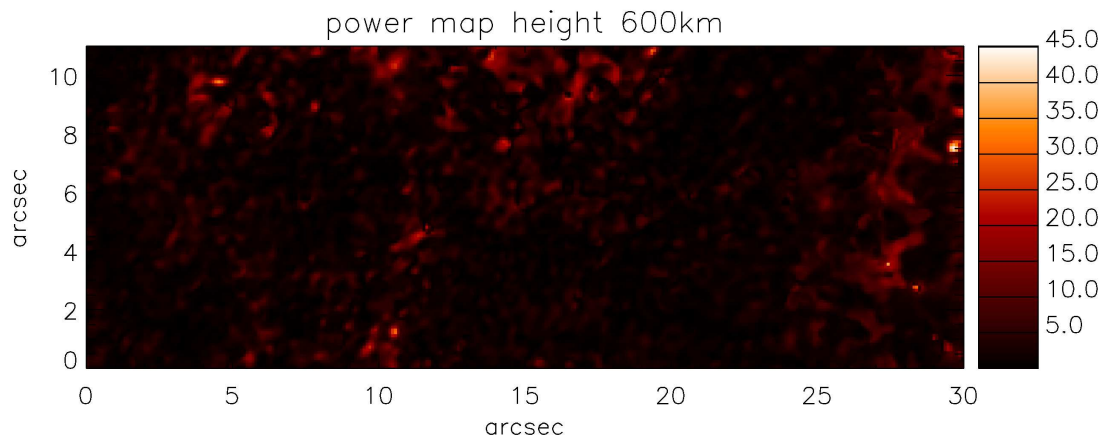


**Fig. 4.** The example of the power map at a height of 600 km, calculated for the data set DS3. The map is corresponding to 113s of the time sequence covered with the data set.

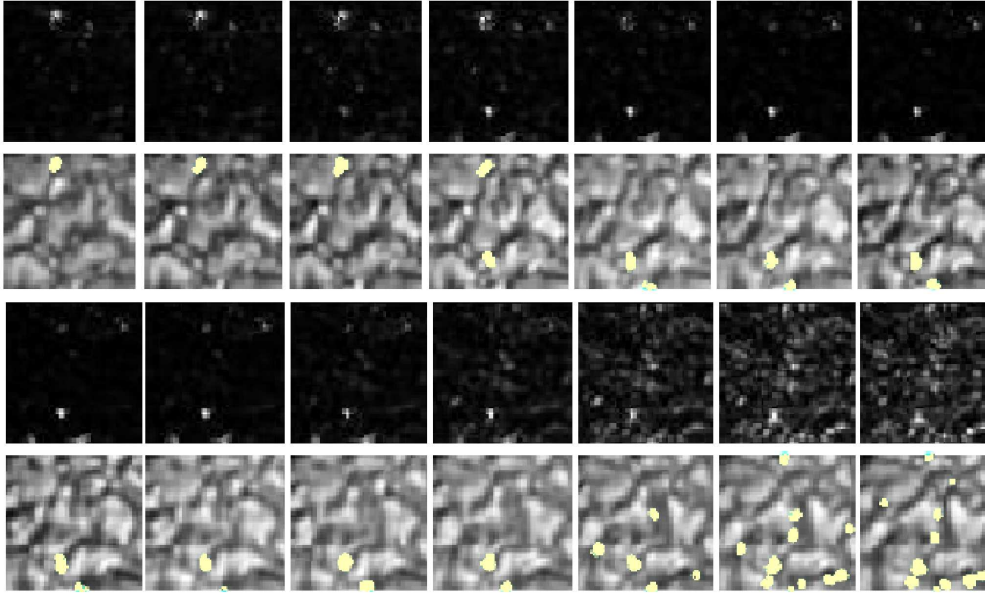


**Fig. 5.** Time sequence of 311.3s in duration from the data set DS4. The evolution of an observed high frequency oscillation is shown. The time goes from left to right and from top to bottom. The time separation between consecutive frames is 28.3s. An oscillation frame and granulation frame below coincide in space and time. The oscillation frames show power of high frequency oscillations integrated over the same period range at a height of 600 km. On the granulation frames the same registered power is overplotted as contour plot. Only power above 0.3 of the maximum power is presented with contour plot so that clarity of the plot can be maximised.

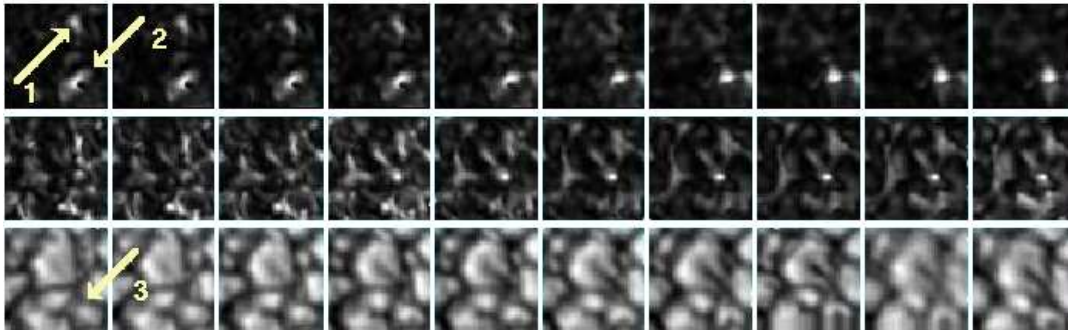


**Fig. 6.** Time sequence of 283s in duration from the data set DS2. The evolution of an observed high frequency oscillation is shown. The time goes from left to right. The time separation between consecutive frames is 28.3s. The top two oscillation frames and granulation frame below coincide in space and time. The top row shows power of high frequency oscillations integrated over the same period range at a height of 600 km, and the bottom row represents granulation changes, the middle row power of high frequency oscillations integrated over frequencies 9 mHz to 18 mHz at a height of 200 km. The arrows 1 and 2 mark the observed oscillation at the beginning of the time evolution. While arrow 3 marks the probable location of the source of oscillations marked with arrow 2.

After this it was necessary to compare the power maps (Fig. 4) with the white-light images (Fig. 2). This was done visually. For accurate spatial comparison the full area of the reconstructed white-light images were cut into squares of  $50 \times 50$  pixels. The same was done for the power maps. The procedure is repeated for each image of the time sequence. In such way the temporal evolution of certain event could be isolated and closely tracked. An example of

the final short temporal sequence obtained in such a way is given in Fig. 6. Then the following procedure is applied:

The observed power was presented in contour plot overplotting the white light images. Only power above 0.3 of the maximum power was taken into account, since this made it possible to pinpoint the sources of stronger oscillations. The power overplotted in such way would be located in the same spa-

cial location as the corresponding granular structure. This made it possible to continue determination of the locations by eye. The spatial comparison done in this way makes it possible to determine the exact location of a power feature in the white-light image. In the first and third row of Fig. 5 one can notice various structures formed by power of high frequency oscillations. I will refer later to such patches as 'power features'. In the second and fourth row the granular evolution is shown; over-plotted are coloured contours which represent areas with observed power due to high frequency oscillations.

To determine if there is a difference in behaviour of oscillations at different frequencies, smaller frequency intervals were used. In Table 2 these periods are listed.

Since wavelet analysis can be used as a band-pass filter (Torrence and Compo 1998), it was optimised to do so. The main frequency range was obtained by integrating the power of high frequency oscillations over all frequencies in the range, for data set DS1 from 11.1 mHz to 20 mHz, for data set DS2 from 8.8 mHz to 17.8 mHz, for data sets DS3 and DS4 from 11.1 mHz to 22.2 mHz and for data set DS5 from 8.4 mHz to 16.9 mHz. Sub ranges stated in Table 2 were obtained by integrating power over the listed sub ranges, thus making it possible to establish variations in behaviour of oscillations over different frequencies.

**Table 2.** Frequency intervals used for analysis.

Data set	abbreviation for interval	frequency range [mHz]
DS1	P11	20-16.7
DS1	P12	16.7-14.3
DS1	P13	14.3-12.5
DS1	P14	12.5-11.1
DS1	P15	11.1-10
DS2	P21	17.8-14.7
DS2	P22	14.7-12.6
DS2	P23	12.6-11.1
DS2	P24	11.1-9.8
DS2	P25	9.8-8.8
DS3,DS4	P31	22.2-18.5
DS3,DS4	P32	18.5-15.8
DS3,DS4	P33	15.8-13.8
DS3,DS4	P34	13.8-12.3
DS3,DS4	P35	12.3-11.1
DS5	P51	16.9-14.1
DS5	P52	14.1-12.1
DS5	P53	12.1-10.5
DS5	P54	10.5-9.3
DS5	P55	9.3-8.4

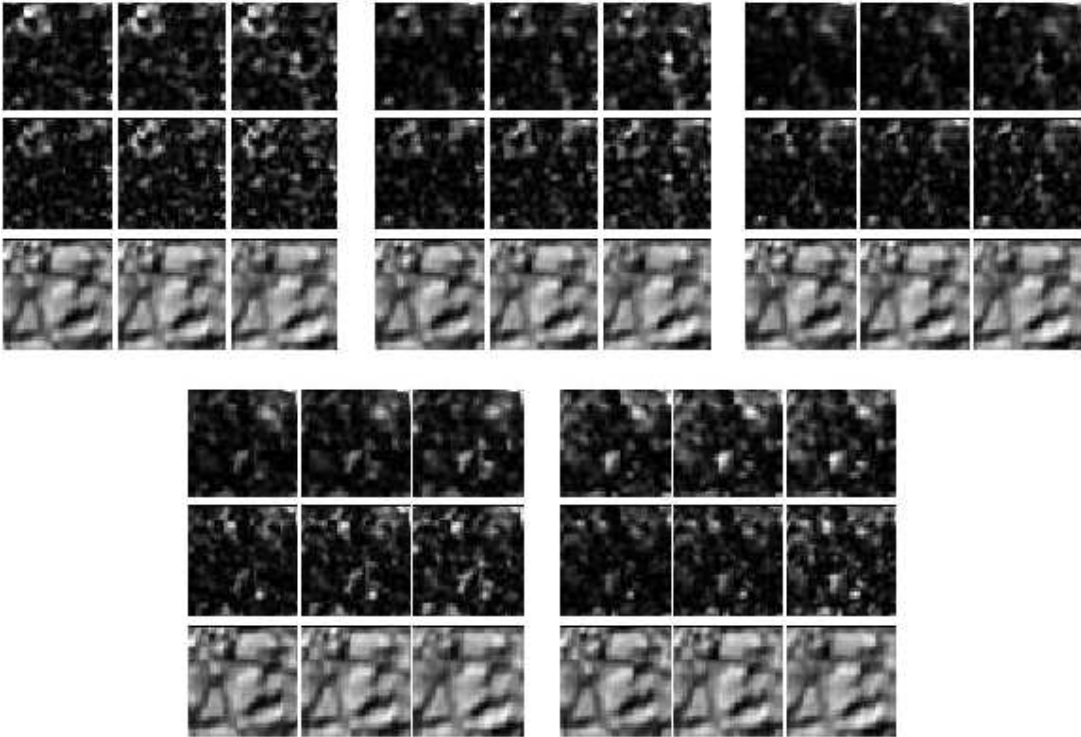


**Fig. 7.** Time sequence of 90s in duration from the data set DS2, in five panels. The evolution of an observed high frequency oscillation is shown. The time goes from left to right. The time separation between consecutive frames is 28.3s. The top two oscillation frames and granulation frame below coincide in space and time. Each panel represents the coinciding interval in time and space. Visible differences on frames which present oscillations are consequence of using different frequency ranges. The five panels represent integrated power over the frequency ranges P21, P22, P23, P24 and P25, at the two different heights of 200 km (middle row) and 600 km (top row).

## 4. RESULTS

### 4.1. Variation of power location with frequencies

The major work in this analysis was done using the image sequences formed on the previously described way (Section 3). The image sequences were made in such way that the evolution of one of the power features can be fully observed. The Figs. 5 - 14 represent short illustrative examples of major results found using this technique.

In Fig. 7 one can easily note differences between various frequencies. The power for different frequency intervals appear, for each interval, at different spatial locations. Usually, the most rapid changes occur for the intervals P13, P23, P23, P34 and P52 (see Table 2), which often do not have much relation to other frequency intervals. In Fig. 7 it can be seen that the intensity of the power in third panel is markedly weakened.

For comparison, Fig. 8 shows the same time sequence with the power integrated over frequency range 18.5 mHz to 9.1 mHz.

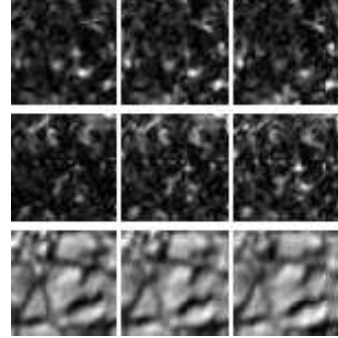


**Fig. 8.** Same time sequence of 90s in duration from data set DS2 as used in Fig. 7, but with the power integrated over the whole frequency range 18.5 mHz to 9.1 mHz.

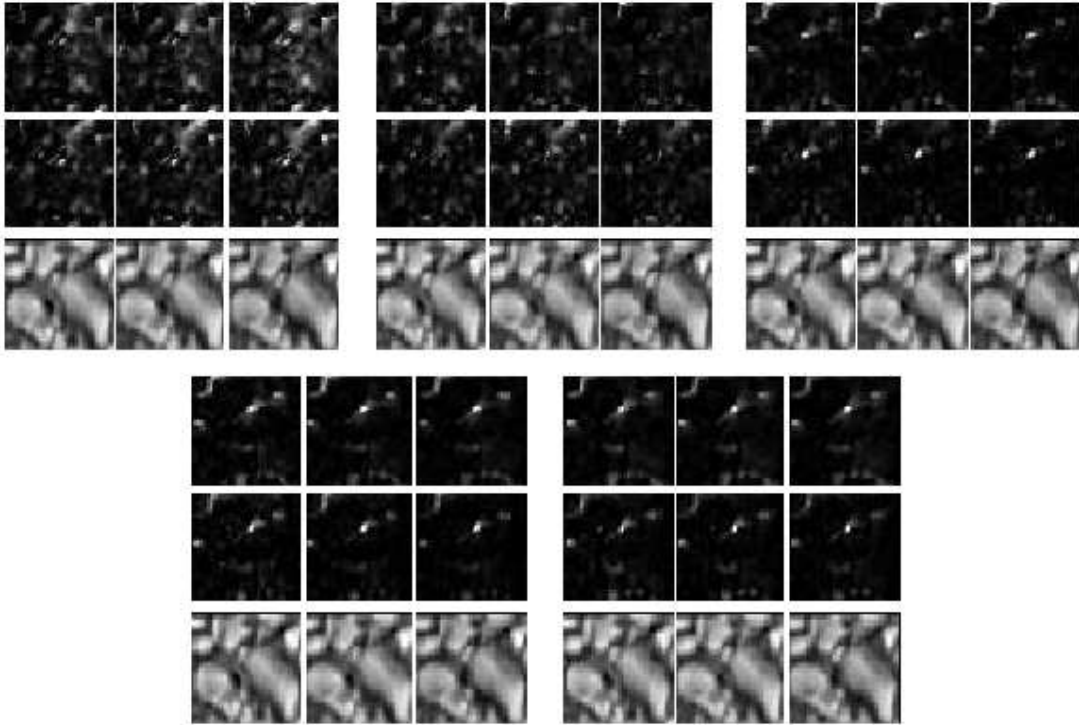


**Fig. 9.** Time sequence of 90s in duration from the data set DS4, in five panels. The evolution of an observed high frequency oscillation is shown. The time goes from left to right. The time separation between consecutive frames is 22.7s. The top two oscillation frames and granulation frame below coincide in space and time. Each panel represents the coinciding interval in time and space. Visible differences on frames which present oscillations are consequence of using different frequency ranges. The five panels represent integrated power over period ranges P21, P22, P23, P24 and P25, at the two different heights of 200 km (middle panel) and 600 km (top panel).

For the data sets containing the quiet Sun, this change of power in the frequency interval around 12.5 mHz is the most obvious. To establish the connection to granulation events a simple statistical analysis of all noted events is done. All observed power features are taken into consideration, regardless of their power intensity. Table 3 gives an overview of the most prominent behaviour of high frequency oscillations with different periods.

**Table 3.** Connection with granulation events: events related to difference in high frequency oscillations visible over the different period ranges, for the quiet Sun.

	Event	%
1	diffuse power features with different shapes over all ranges	43
2	change of the location over the frequency range around 12.5mHz	27
3	diffuse power features with similar shapes over all ranges	13
4	no differences	7
5	maximums at different locations	4

The event No.1 happened together with slow granular changes, while event No.3 relates to changes of small structures. The variation of the location of maximums, event No. 5, is found in relation with different granular events. In 4% of the cases where a variation over period ranges occurs, one can find that power in P11, P21, P21, P31 and P51 has a different location compared with P14, P24, P24, P54 and P74. In contrast P15, P25, P25, P35 and P55 show power at the same locations, as in the former two period ranges.

Almost all granular changes tend to produce high frequency oscillations regardless of their frequency. Yet it is observed that certain granulation events (e.g. exploding granule) which repeat in the field of view and evolve during the observing interval, usually produce high frequency oscillations of differing frequencies.

The exact sources of high frequency oscillations could not be resolved with the achieved spatial resolution. So, there is no clear correlation between the resolved granular events and the appearance of high frequency oscillations over the different frequency intervals in the quiet Sun data.

For the G-band data there is some difference as compared to the quiet Sun observations. In Fig.

10 the behaviour above bright point structure is presented. In Fig. 9 one can see in different sub-panels the power in the different frequency intervals. It is easy to notice that the first two panels, which present power in the intervals P21 and P22, show significant differences in comparison with the other three panels.

It can also be seen in Fig. 10 that power appears in all frequency intervals. Comparison of those two figures shows that in this example some power of the high frequency ranges P21 and P22 does not occur when integrated over the whole period range. This clearly indicates that in this case the power in those two intervals is much smaller than in the other three intervals. Some consequences of this fact are also mentioned and discussed in (Andic 2005).

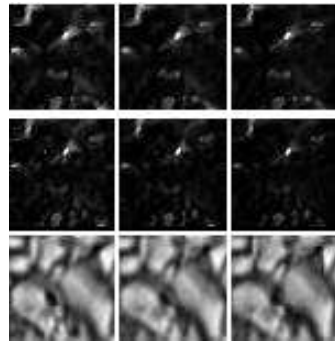


**Fig. 10.** The time sequence of 90 of the same granular change seen in data set DS4 presented in Fig. 9, but for integrated power over the whole period range.

In Table 4 an overview of the behaviour of power features in different frequency intervals is given, as for the quiet Sun regions.

It is seen, from Table 4, that for the data near G-band structures more diffuse power features appear. This pattern is usually caused by changes of small granulation structures. In the data set, DS4, there is a bright-point-like structure, in the same spatial location trough out frequency ranges. In the rest of the cases a slightly larger power is observed in the different frequency intervals compared to the integrated power.

In the data sets containing a pore, in locations outside the pore the analysis leads to similar results as for the data sets with G-band structures. Therefore only the power features directly above the pore and its immediate vicinity were analysed.

**Table 4.** Events related to differences in the high frequency oscillations visible over the different period ranges, for the G-band structures.

	Event	%
1	similar diffuse power features over all ranges	28
2	change in the position over the range of 70 to 80s	14
3	similar diffuse power features over all ranges	17
4	no differences	13
5	maximums at different locations	25

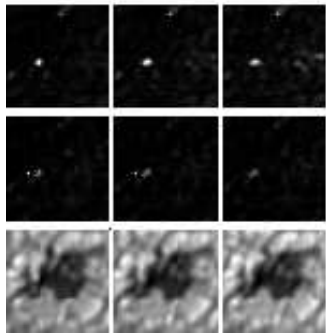


**Fig. 11.** *The time sequence of 90 of the same granular change for the data set DS<sub>4</sub> presented in Fig. 12, but for the integrated power over the whole period range.*

In Fig. 12 the power integrated over all periods is presented. It can be seen that the location

of the strong maximum correspond for both levels, whereas the rest of the power is insignificant.

The appearance of power related to the bright-point-like structures in the pore is more extreme. One finds no variation in power over the frequency intervals. The comparison of Figs. 11 and 12 clearly illustrate this. Some variations can be found in Fig. 12, but in comparison with the previous sets of data those variations can be ignored.

#### 4.2. Comparison of high frequency oscillations to oscillations of lower frequency

To complete the discussion about differences in the various frequency intervals I here discuss a comparison between the high and low frequency oscillations. Such a comparison is only done for the data sets from the quiet Sun. In this work I use conclusions from previous works which were analysing the lower frequency oscillations, e.g. (Espagnet et al. 1992). The presented results are in agreement with this work.

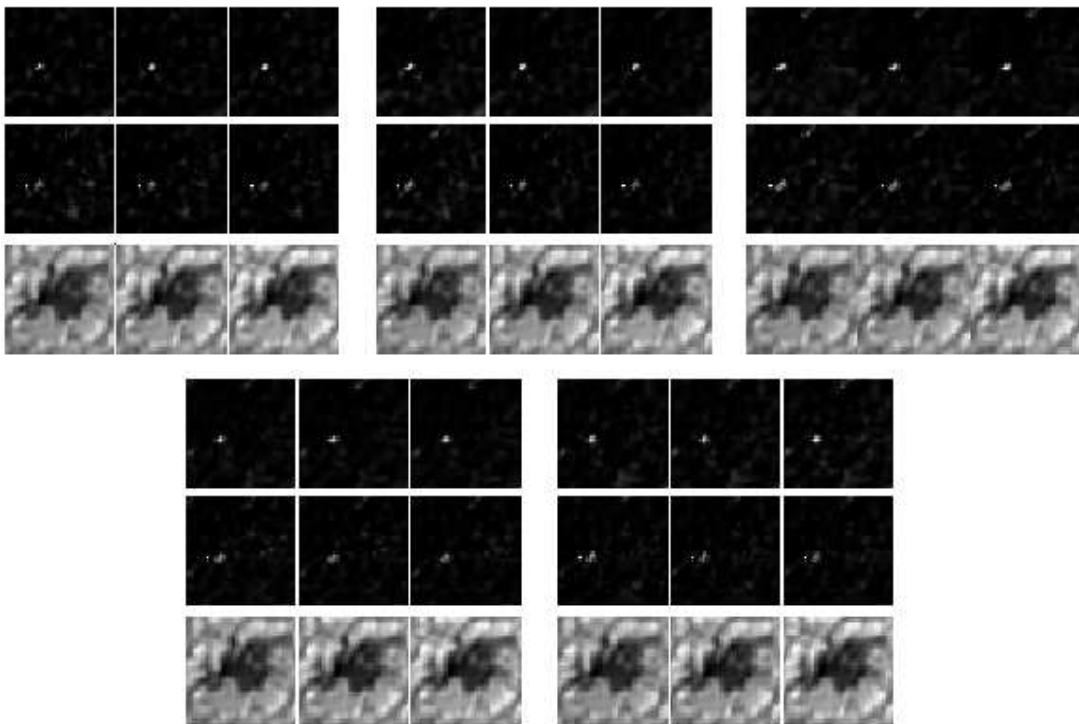


**Fig. 12.** *Time sequence of 90s in duration from the data set DS<sub>4</sub>, in five panels. The evolution of an observed high frequency oscillation is shown. The time goes from left to right. The time separation between consecutive frames is 22.7s. The top two oscillation frames and granulation frame below coincide in space and time. Each panel represents the coinciding interval in time and space. Visible differences on frames which present oscillations are consequence of using different frequency ranges. The five panels represent integrated power over period ranges P<sub>21</sub>, P<sub>22</sub>, P<sub>23</sub>, P<sub>24</sub> and P<sub>25</sub>, at the two different heights of 200 km (middle panel) and 600 km (top panel).*

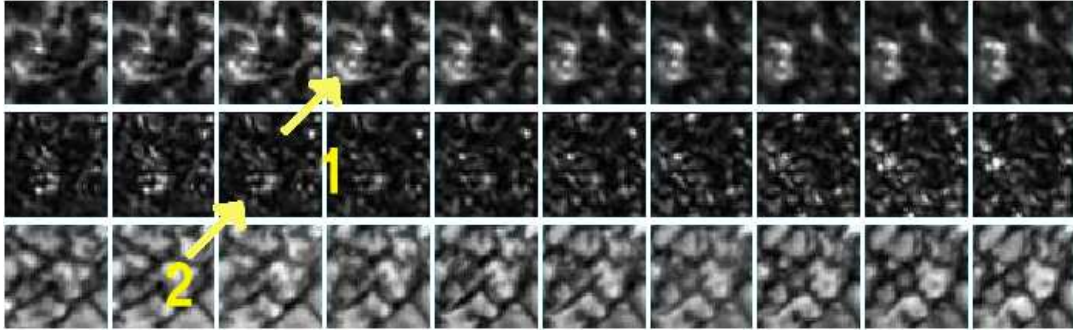


**Fig. 13.** Time sequence of 250s in duration from the data set DS1. The evolution of an observed high frequency oscillation is shown. The time goes from left to right. The time separation between consecutive frames is 25s. The top two oscillation frames and granulation frame below coincide in space and time. The top panel represents power integrated over range 5 mHz to 20 mHz, the middle one power integrated over the range 10 mHz to 20 mHz, both at the height of 600 km; the bottom panel represents the corresponding granulation change.

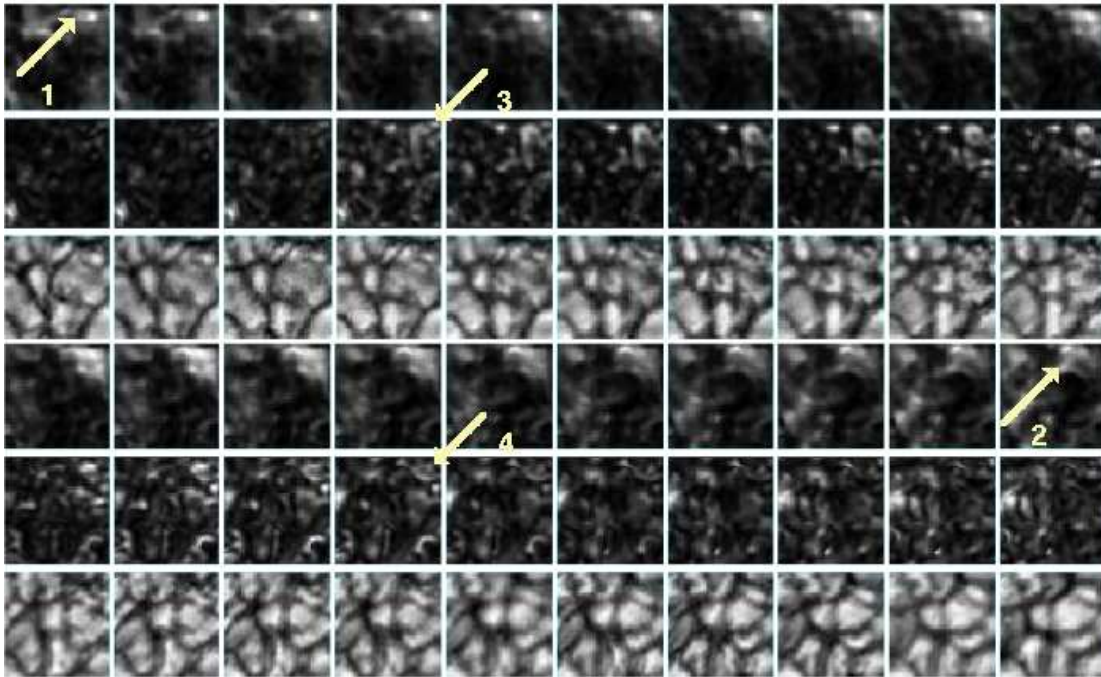


**Fig. 14.** Time sequence of 500s in duration from the data set DS1. The evolution of an observed high frequency oscillation is shown. The time goes from left to right. The time separation between consecutive frames is 25s. The top two oscillation frames and granulation frame below coincide in space and time. The top row represents power integrated over the range 5 mHz to 20 mHz, the middle one power integrated over the range 10 mHz to 20 mHz, both at the height of 600 km; the bottom row represents the corresponding granulation change.

#### 4.3. The range of 5 to 20 mHz

For the same data set, DS1, wavelet analysis was done two times to yield two sets of power maps integrated over the frequency intervals 10 mHz to 20 mHz and 5 mHz to 20 mHz. The differences in the features occurring in both intervals are evident from the analysis. The examples and observed character-

istics are illustrated with Figs. 13 and 14. They also indicate more power in the range 5 mHz to 10 mHz than in the range 10 mHz to 20 mHz, since no structure from the interval 10 mHz to 20 mHz is visible in the power maps.

Fig. 13 presents the variation of power features over different frequency intervals. It is apparent that features of longer period oscillations tend to vary more slowly and cluster near specific locations.

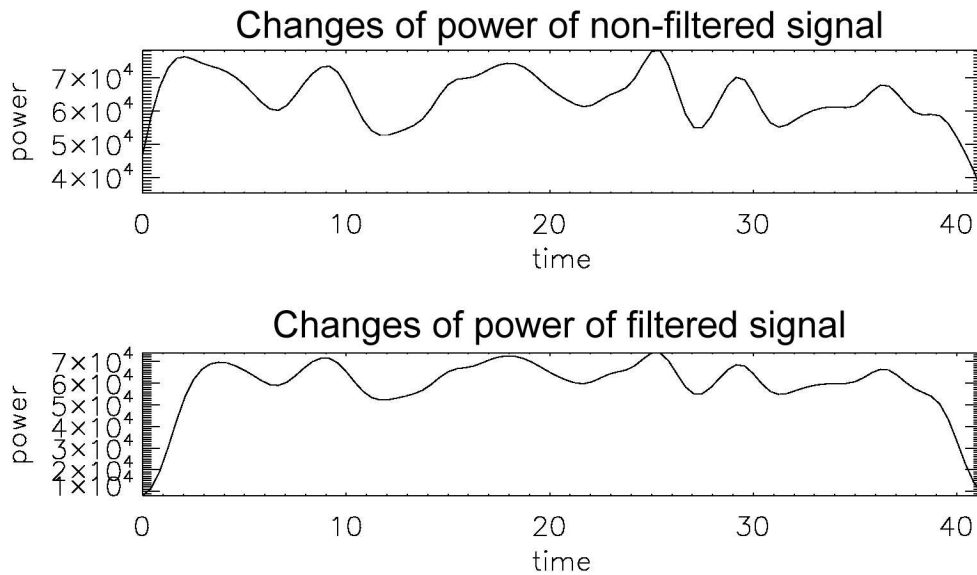


**Fig. 15.** Temporal changes of high frequency oscillations. Top panel represents power of the non filtered signal, and the bottom power of the signal filtered with the high pass Fourier filter.

The event which illustrated this behaviour is marked 1. Power features of high frequency oscillations are more diffuse, and seem to originate from larger numbers of smaller sources, marked with 2.

In Fig. 14 the behaviour of features with maximum intensity is shown. Arrows 1 and 2 mark the maximum of the longer period oscillations, and arrows 3 and 4 mark the maximum of the high frequency oscillations. Both maximums appear at the same location.

Careful inspection shows that the features of longer period oscillations appear earlier in time sequence and last longer than the corresponding feature of high frequency oscillations at the same location. In turn, the power features of high frequency oscillations appear later and their maximums follow the granular changes which could be a cause of the power.

#### 4.4. The frequency range between 3 mHz and 6 mHz

Also for the data set DS5a wavelet analysis was done two times yielding power maps integrated over the frequency intervals 11 mHz to 22 mHz and 3 mHz to 22 mHz. For this set of data, power integrated over the whole range from 3 mHz to 22 mHz shows a dominant power feature in the range 11 mHz to 22 mHz, indicating that oscillations in this period interval have the largest amplitudes. Therefore it was necessary to separate this range (11 mHz to 22 mHz), from the one between 3 mHz and 6 mHz. The cause of this behaviour could not be determined.

The power maps of this range show behaviour of the longer period oscillations to be similar to the behaviour of the oscillations in the interval 5 mHz to 10 mHz. The changes of their power features are

slower and they do not come from the same sources as the high frequency oscillations.

The maximums of the wave power behave similarly as in Fig. 14. The power features of longer period oscillations last longer than the corresponding power features of high frequency oscillations at the same location.

#### 4.5. The modulations of total power of the high frequency oscillations

To check if the low frequency oscillations have some influence on the power of high frequency oscillations, a summation of the power maps is done. Following figures show that the power of high frequency oscillations is influenced with low frequency oscillations. To double check this finding, double filtering was performed.

The top panel of Fig. 15 shows the modulation of the power maps obtained with wavelet analysis over non filtered data, and the bottom panel shows the modulation of the power maps obtained from the data which were first filtered with a high pass Fourier filter. It is easy to notice that the influence of the long period oscillations could not be removed with the filter.

## 5. DISCUSSION AND CONCLUSIONS

The high frequency oscillations tended to vary with frequency interval. Those variations are more rapid than the changes of observed granulation events. The similar granulation events also tended to cause oscillation frequencies within different frequency ranges.

In comparison with lower frequency oscillations, the difference in behaviour is more pronounced. High frequency oscillations tend to appear after low frequency ones and last for a shorter time. High frequency oscillations also cover smaller spatial areas than low frequency ones.

Data sets used in this work were obtained by observing of the Fe I neutral spectral line at 543.45 nm, with the post-focus equipment made specifically following the demands of speckle reconstruction. The speckle reconstruction process tended to introduce around 10% error into the data (von der Lühe 1984, 1993, and 1994). When recommendations for noise filter settings are followed (von der Lühe 1984, 1993, 1994 and de Boer 1996). The influence of seeing effects is mainly visible during speckle reconstruction, since when seeing is too bad the procedure can not be completed.

The calculation of velocity response functions tended to increase the noise in the velocity maps. The combinations of different images increase the noise level in the resulting image. To minimise this increase in noise, only two linear combinations of velocity response functions are used, resulting in the two height levels 200 km and 600 km. Linear combinations for the heights in between those two levels would require the use of three velocity response functions (i.e. three images); while linear combinations for heights below 200 km and above 600 km would require even more. The noise level was assessed using the wavelets and the band pass Fourier filter. In cases where three linear combinations were used, the amount of observed high frequency oscillations was decreased. This trend increased with the increasing number of linear combinations. Additional check were performed on the oscillations in the range 3 mHz to 6 mHz, since that range is well known. The velocity maps showed similar behaviour pointing to the increase of noise level as a possible explanation. Nevertheless, this added noise was taken care of by wavelet analysis since wavelet analysis has proved to be an excellent noise reduction filter (Torrence and Compo 1998). The final influence seeing had on the data set is in image cadence. In the case of average atmospheric conditions (allowing the use of the adaptive optics (Berkefeld and Soltau 2001, Soltau et al. 2002)) the number of the images per position was increased, and in the case of very good or excellent seeing, the number of images per position was reduced, allowing for faster cadence of the whole data set. This procedure resulted in similar noise levels after data reduction for the all data sets.

In the Section 4.5 the influence of low frequency oscillations was mentioned. Unfortunately it is not very clear how much this effect is produced by Fourier analysis itself since it tends to smear power over the whole analysed range. In the wavelet analysis technique I used, the use of Fourier space was necessary to speed up necessary calculations. Therefore the exact influence of Fourier analysis could not be isolated and corrected for.

It is noticeable that the connection between various frequency intervals cannot be observed, nor its clear connection with the granulation event which presumably caused it. Also the power tends to vary

with frequency. Sometimes the power is pronounced around one frequency and sometimes around another. Again no clear connections with the granulation events was observed. The most often change was happening around the frequency 13 mHz. A reduction in power is also observed around this frequency and is most noticeable for the data sets with the quiet Sun as the object of observation. The cause of this event is not clear.

The difference for the data sets with G-band structures was the most pronounced with the appearance of power above the bright-point structure. The power features in those locations tended to keep their shape and position for most of the frequency ranges investigated. A possible explanation for this can be found in magnetic influences. Acoustic oscillations tend to change into magneto-acoustic oscillations in areas where the magnetic field should be present (Espagnet et al. 1992, Ulmschneider and Kalkofen 2002, Ulmschneider 2003). Around the G-band structures one expects a flux tube, in which, the analogue to the ordinary acoustic wave is the longitudinal tube wave. They are very similar to acoustic oscillations and develop into shocks, which heat the tubes by dissipating the wave energy. The methods used in this work allow us to register those types of oscillations as well, yet additional analysis has to be performed (more results and analysis techniques will be published in the next paper). The main influence of the magnetic field comes from its geometric shape which channels the propagating wave. This can explain why the shape of the power feature tends to remain the same over different frequencies.

The second most common event for the data with G-band structures is the more diffuse power features which appear in the vicinity of G-band structures. This pattern is usually connected with changes of abnormal granulation. The cause of this could be simple merging of the oscillations as predicted in work by Ulmschneider (2003).

The appearance of power features above the pore and its immediate vicinity gives more indication that the magnetic field and its accompanying flux tubes have a significant influence. The location of the strong maximum correspond for both height levels, regardless of expected changes to the power features due to an expansion of high frequency oscillations travelling upwards. More detailed analysis of this will be published in the next paper. Also, the appearance of power related to bright-point-like structures in the pore is more extreme. One finds no variation of power over the frequency intervals. Also there is a significant reduction in the amount of observed power above the pore itself. The total observed power above the pore and in its immediate vicinity tended to be significantly less than the power observed above other objects of observation.

The variation of oscillatory behaviour over the different frequencies is in agreement with the works by Ulmschneider (1971a,b), Kalkofen (1990, 2001), Ulmschneider and Kalkofen (2002) and Ulmschneider (2003).

Compared to oscillations of much lower frequencies, it shows different appearance and behaviour as that of high frequency oscillations. Work

by Espagnet et al. (1992), finds that lower frequency oscillations are located in the intergranular lanes and that their source is deeply located in the granulation layer. The present results for the lower frequency oscillations confirms that finding: the appearance of power in intergranular lanes has slow temporal evolution, and a tendency for the power maximum to appear after the maximum of temporal variation of the white-light structure.

High frequency oscillations are located in similar areas as lower frequency oscillations, however, temporal evolution appears differ. High frequency oscillations tend to appear later than lower frequency oscillations and more abruptly. The maximum of power features tends to follow more closely the temporal evolution of white-light structures with which it can be associated with. Another observed difference is the power features of higher frequency oscillations show an indication of different sources since they appear as more edge defined and less merged when compared to power features from lower frequency oscillations.

Both of these findings indicate that high frequency oscillations are formed closer to the solar surface than low frequency ones. The different frequencies are associated with different spatial scales. Again, comparing to work which describes the generation of oscillations (Lighthill 1951, Proudman 1952, Stein 1967, Stein and Leibacher 1974) it is clear that such behaviour is expected. The frequency of the emitted wave depends on the fluid flow, as different characteristics cause different emitted frequencies. Besides it is also predicted in previous work that oscillations of different frequencies should behave differently which is in agreement with observations in presented here. It would be interesting to try to determine exact sources of oscillations of different frequencies when development of observing equipment becomes advanced enough to allow the necessary spacial resolution.

*Acknowledgements* – First and most, I wish to thank F. Kneer for all constructive comments and dialogues and directing to the appropriate literature. I wish to thank P. Sutterlin and K. Janssen for giving me software for data reduction.

During the work itself, I had lots of stimulating discussions for which I wish to thank R. Cameron, A. Vögler and E. Wiehr. For the help with the observations I wish to thank J.K. Hirzberger, M. Wunnenberg and K.G. Puschmann.

Also I wish to thank D.B.Jess for help with the English.

## REFERENCES

- Andic, A.: 2005, *Solar Phys.*, submitted.
- Bendlin, C., Volkmer, R., Kneer, F.: 1992, *Astron. Astrophys.*, **257**, 817.
- Berkefeld, Th., Soltau, D., Venice 2001, Beyond Conventional Adaptive Optic.
- de Boer, C.R., Kneer, F.: 1994, *IAU Symp.*, **158**, 398D.
- de Boer, C.R., Kneer, F., Nesis, A.: 1992, *Astron. Astrophys.*, **257**, L4-L6.
- Deubner, F.L., Laufer, J.: 1983, *Solar Phys.*, **82**, 151D.
- Domínguez, I.F.: 2004, PhD Thesis, Goettingen University.
- Eibe, M.T., Mein, P., Roudier, Th., Faurobert, M.: 2001, *Astron. Astrophys.*, **371**, 1128.
- Espagnet, O. et al.: 1996, *Astron. Astrophys.*, **313**, 297.
- Hansteen, V.H., Betta, R., Carlsson, M.: 2000, *Astron. Astrophys.*, **360**, 742.
- Hoekzema, N.M., Rimmele, T.R., Rutten, R.J.: 2002, *Astron. Astrophys.*, **390**, 681.
- Holweger, H., Müller, E.A.: 1974, *Solar Phys.*, **39**, 19.
- Janssen, K.: 2003, Ph.D. Thesis, Goettingen University.
- Kalkofen, W.: 2001, *Astrophys. J.*, **557**, 376.
- Kalkofen, W.: 1990, *IAU Symp.*, **142**, 197K.
- Keller, C.U., von der Lühe, O.: 1992, *Astron. Astrophys.*, **261**, 321.
- Koschinsky, M., Kneer, F., Hirzberger, J.: 2001, *Astron. Astrophys.*, **365**, 588.
- Lighthill, M.J.: 1951, Proceedings of the Royal Society, A, **211**, p. 564.
- Moretti, P.F. et al.: 2001, *Astron. Astrophys.*, **372**, 1038.
- November, L.J.: 1986, *Applied Optic*, **25**, 3, 392.
- Pérez Rodríguez, E., Kneer, F.: 2002, *Astron. Astrophys.*, **395**, 279.
- Proudman, I.: 1952, Proceedings of the Royal Society of London, A, **214**, 119.
- Soltau, D., Berkefeld, Th., von der Luehe, O., Woeger, F., Schelenz, Th.: 2002, *Astron. Nachr.*, **323**, 3/4, 236-240.
- Stein, R.F.: 1967, *Solar Phys.*, **2**, 385S.
- Stein, R.F., Leibacher, J.: 1974, *Astron. Astrophys.*, **12**, 407.
- Torrence, C., Compo, G.P.: 1998, *Bull. Amer. Meteor. Soc.*, **79**, 61.
- von Uexküll, M., Kneer, F., Mattig, W., Nesis, A., Schmidt, W.: 1985, *Astron. Astrophys.*, **146**, 192.
- Ulmschneider, P.: 2003, Lectures in solar Physic, H.M. Antia, Springer and Verlag.
- Ulmschneider, P., Kalkofen, W.: 2002, Dynamic Sun, B.N. Dwivedi, Ed., Cambridge University Press.
- Ulmschneider, P.: 1971, *Astron. Astrophys.*, **14**, 275.
- Ulmschneider, P.: 1971, *Astron. Astrophys.*, **12**, 297.
- Vernazza, J.E., Avrett, E.H., Loeser, R.: 1981, *Astrophys. J.*, **45**, 635.
- Wunnenberg, M., Kneer, F., Hirzberger, J.: 2003, *Astron. Astrophys.*, **271**.
- Wunnenberg, M., Andjic, A., Kneer, F.: 2003, *Astron. Nachr.*, **324**, 4, 356.
- Yi, Z., Molowny Horas, R.L.: 1992, in: Proc. from LEST Mini-workshop, Software for solar image processing, eds. Z. Yi, T. Daravann, R. Molowny Horas, Oslo ITA, 69.

**ОДНОС ОСЦИЛАЦИЈА У ФРЕКВЕНЦИОНОМ ОПСЕГУ  
3.6 mHz ДО 22 mHz У СУНЧЕВОЈ ХРОМОСФЕРИ**

**A. Anđić<sup>1,2</sup>**

<sup>1</sup>*Institut für Astrophysik,  
Friedrich-Hund-Platz 1, 37077 Göttingen, Germany*

<sup>2</sup>*Faculty of Sciences,  
M. Stojanovića 2, 78000 Banja Luka, Bosnia and Herzegovina*

UDK 523.945-78

*Оригинални научни рад*

Високофреквенционе акустичне осцилације су предложене као извор механичког грејања у хромосфери. У овом раду само је радијална компонента осцилација у фреквенционом интервалу 3 mHz до 22 mHz испитивана. Посматрања су обављена користећи 2D спектрометрију са Fe I неутралном спектрал-

ном линијом (543.45 nm). Високофреквенционе осцилације различитих фреквенција се могу повезати са различитим просторним скалама. Резултати указују на могућност да различити извори производе осцилације високих и ниских фреквенција.